

Controlling Magnetic Order, Magnetic Anisotropy, and Band Topology in Semimetals Sr(Mn_{0.9}Cu_{0.1})Sb₂ and Sr(Mn_{0.9}Zn_{0.1})Sb₂

Farhan Islam,¹ Renu Choudhary,¹ Yong Liu,^{1,2} Benjamin G. Ueland,¹ Durga Paudyal,¹ Thomas Heitmann,³ Robert J. McQueeney,⁴ and David Vakhnin^{4,*}

¹Ames Laboratory, Iowa State University, Ames, Iowa 50011, USA

²Crystal Growth Facility, Institute of Physics, The École Polytechnique Fédérale de Lausanne, CH-1015 Lausanne, Switzerland

³The Missouri Research Reactor, University of Missouri, Columbia, Missouri 65211, USA

⁴Ames Laboratory, and Department of Physics and Astronomy, Iowa State University, Ames, Iowa 50011, USA

(Dated: September 1, 2020)

Neutron diffraction and magnetic susceptibility studies show that orthorhombic single-crystals of topological semimetals Sr(Mn_{0.9}Cu_{0.1})Sb₂ and Sr(Mn_{0.9}Zn_{0.1})Sb₂ undergo three dimensional C-type antiferromagnetic (AFM) ordering of the Mn²⁺ moments at $T_N = 200 \pm 10$ and 210 ± 12 K, respectively, significantly lower than that of the parent SrMnSb₂ with $T_N = 297 \pm 3$ K. Magnetization versus applied magnetic field (perpendicular to MnSb planes) below T_N exhibits slightly modified de Haas van Alphen oscillations for the Zn-doped crystal as compared to that of the parent compound. By contrast, the Cu-doped system does not show de Haas van Alphen magnetic oscillations, suggesting that either Cu substitution for Mn changes the electronic structure of the parent compound substantially, or that the Cu sites are strong scatterers of carriers that significantly shorten their mean free path thus diminishing the oscillations. Density functional theory (DFT) calculations including spin-orbit coupling predict the C-type AFM state for the parent, Cu-, and Zn-doped systems and identify the a -axis (i.e., perpendicular to the Mn layer) as the easy magnetization direction in the parent and 12.5% of Cu or Zn substitutions. In contrast, 25% of Cu content changes the easy magnetization to the b -axis (i.e., within the Mn layer). We find that the incorporation of Cu and Zn in SrMnSb₂ tunes electronic bands near the Fermi level resulting in different band topology and semi-metallicity. The parent and Zn-doped systems have coexistence of electron and hole pockets with opened Dirac cone around the Y-point whereas the Cu-doped system has dominant hole pockets around the Fermi level with a distorted Dirac cone. The tunable electronic structure may point out possibilities of rationalizing the experimentally observed de Haas van Alphen magnetic oscillations.

I. INTRODUCTION

SrMnSb₂ belongs to a class of bulk topological semimetals ($AMnPn_2$; $A = \text{Sr, Ba, Ca}$; $Pn = \text{Sb and Bi}$) where Sr-Sb layers are predicted to host Dirac fermions [1–6]. The degeneracy of the Dirac bands can be removed by breaking either time-reversal symmetry (TRS) or inversion symmetry to produce Weyl fermions in the bulk of these systems. Time reversal symmetry can be broken by a magnetic field (internally or externally applied) which makes this class of materials intriguing as they possess exchange-coupled Mn²⁺ layers, albeit, Mn-Mn coupling is primarily antiferromagnetic (AFM) and requiring net ferromagnetism (FM) to break the average TRS at the Sb site [7]. It has been reported that Mn- and Sr-deficiencies in Sr_{1-y}Mn_{1-z}Sb₂ with $y \sim 0.08$ and $z \sim 0.02$ can generate a spontaneous spin canting that gives rise to weak-ferromagnetism [8]. As a result, Sr_{1-y}Mn_{1-z}Sb₂ is reportedly a Weyl semimetal that emerges by subjecting the Dirac fermions to a broken TRS via weak FM ordering [8]. Subsequent studies have reported much weaker or even absent FM in the stoichiometric SrMnSb₂ [9, 10].

Based on the interest to understand the role of defects,

and the capability of carrier doping to tune topological semimetals, we recently reported neutron diffraction and magnetic susceptibility studies of hole-doped single crystal (Sr_{0.97}K_{0.03})MnSb₂ confirming the three-dimensional (3D) C-type type AFM ordering of the Mn²⁺ moments at a slightly higher Néel temperature (T_N) than that of the parent SrMnSb₂. These compounds form checkerboard-like AFM layers that are stacked ferro-magnetically, as shown in Fig. 1 (a). de Haas van Alphen (dHvA) oscillations can provide a sensitive probe of the Fermi sur-

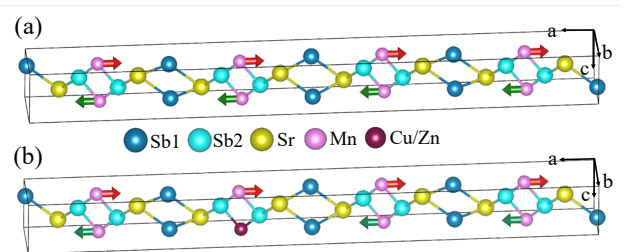


FIG. 1: Chemical and C-type AFM spin structure showing a $2 \times 1 \times 1$ -supercell of (a) parent SrMnSb₂ and (b) 12.5% Cu/Zn-doped SrMnSb₂. Red and green arrows on Mn-atoms represent the spin direction of Mn moment along the a -axis. Note that this $Pnma$ orthorhombic structure has a long a -axis with planes of MnSb in the bc -basal plane.

*Electronic address: vakhnin@ameslab.gov

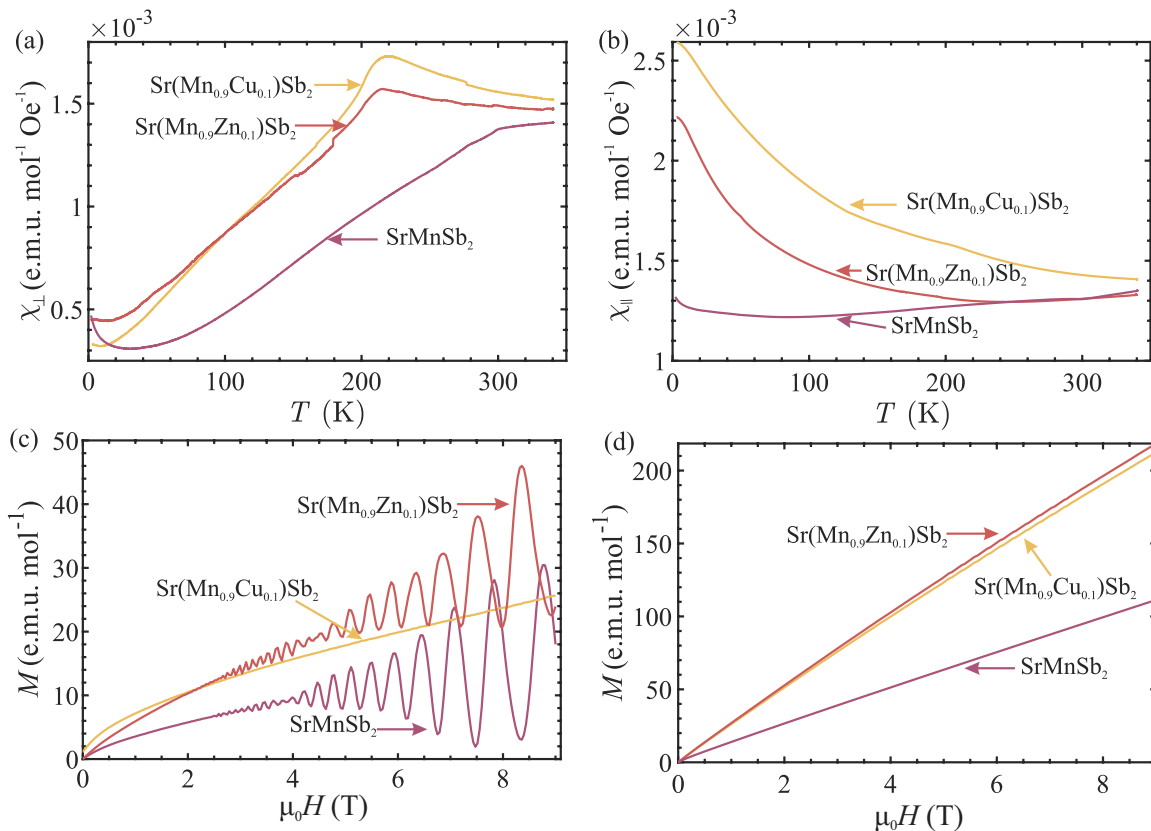


FIG. 2: Comparison of magnetic properties of parent compound SrMnSb_2 with doped $\text{Sr}(\text{Mn}_{0.9}\text{Zn}_{0.1})\text{Sb}_2$ and $\text{Sr}(\text{Mn}_{0.9}\text{Cu}_{0.1})\text{Sb}_2$. Temperature dependence of magnetic susceptibility is shown with both (a) H perpendicular to the MnSb planes $\chi_{\perp}(T)$ and (b) with H in the MnSb planes $\chi_{\parallel}(T)$. (c) Magnetization versus applied field perpendicular to the MnSb planes M_{\perp} at $T = 2$ K showing de Haas van Alphen (dHvA) oscillations for the parent and $\text{Sr}(\text{Mn}_{0.9}\text{Zn}_{0.1})\text{Sb}_2$ compounds but not for $\text{Sr}(\text{Mn}_{0.9}\text{Cu}_{0.1})\text{Sb}_2$. (d) Magnetization versus applied field in the MnSb planes H_{\parallel} at $T = 2$ K exhibiting linear field dependence as expected from an AFM system with moments that are aligned perpendicular to the applied field.

face geometry and are extensively used to characterize topological semimetals. In $(\text{Sr}_{0.97}\text{K}_{0.03})\text{MnSb}_2$, magnetization versus applied magnetic field exhibits dHvA oscillations with a slight frequency shift as compared to the parent compound, presumably due to hole doping of the system [11]. Here, we examine the effect of Cu and Zn substitutions of the Mn site - i.e., $\text{Sr}(\text{Mn}_{0.9}\text{Cu}_{0.1})\text{Sb}_2$ and $\text{Sr}(\text{Mn}_{0.9}\text{Zn}_{0.1})\text{Sb}_2$ - by employing single-crystal neutron diffraction techniques and magnetic measurements. We find that the T_N is significantly lower in these systems compared to their parent compound. Moreover, whereas SrMnSb_2 , $(\text{Sr}_{0.97}\text{K}_{0.03})\text{MnSb}_2$, and $\text{Sr}(\text{Mn}_{0.9}\text{Zn}_{0.1})\text{Sb}_2$ show dHvA oscillations, $\text{Sr}(\text{Mn}_{0.9}\text{Cu}_{0.1})\text{Sb}_2$ does not.

We also report DFT calculations incorporating spin-orbit couplings to track the effects of Cu and Zn substitution of Mn on the band structure to rationalize their experimentally observed distinct behaviors. Previous band structure calculations combined with ARPES have shown that the vicinity of the Y-point of SrMnSb_2 has small Fermi pockets with linearly dispersing bands [9]. These pockets give rise to the dHvA oscillations in SrMnSb_2 . Therefore, we focus our DFT calculations on the effect that Cu or Zn substitutions for Mn have on the

Y-point. Indeed, we find that Zn substitution does not significantly affect the Y-point of the parent compound, whereas Cu substitution does.

II. EXPERIMENTAL DETAILS AND METHODS

Plate-like single crystals of $\text{Sr}(\text{Mn}_{0.9}\text{Cu}_{0.1})\text{Sb}_2$ and $\text{Sr}(\text{Mn}_{0.9}\text{Zn}_{0.1})\text{Sb}_2$ were grown by a self-flux method. Cu and Zn substituted samples were prepared from a starting molar ratio of Sr:Mn:Cu(Zn):Sb=1:0.9:0.1:4. The strontium dendritic pieces, manganese powder, copper powder, zinc pellets, and antimony chunks were weighed and loaded into alumina crucible in a glovebox. The alumina crucible was sealed in an evacuated quartz tube with backfilling 300 mbar Ar gas. The quartz ampoule was heated up to 1073 K. After a dwell of 6 hours, it was cooled down to 773 K at a cooling rate of 3 K/h. Then the furnace was switched off. The centimeter-sized plate-like single crystals were mechanically separated from the matrix. More details can be found in Ref. [10]. The Cu and Zn content was determined by Energy-dispersive X-ray spectroscopy (EDS) measurements, which is con-

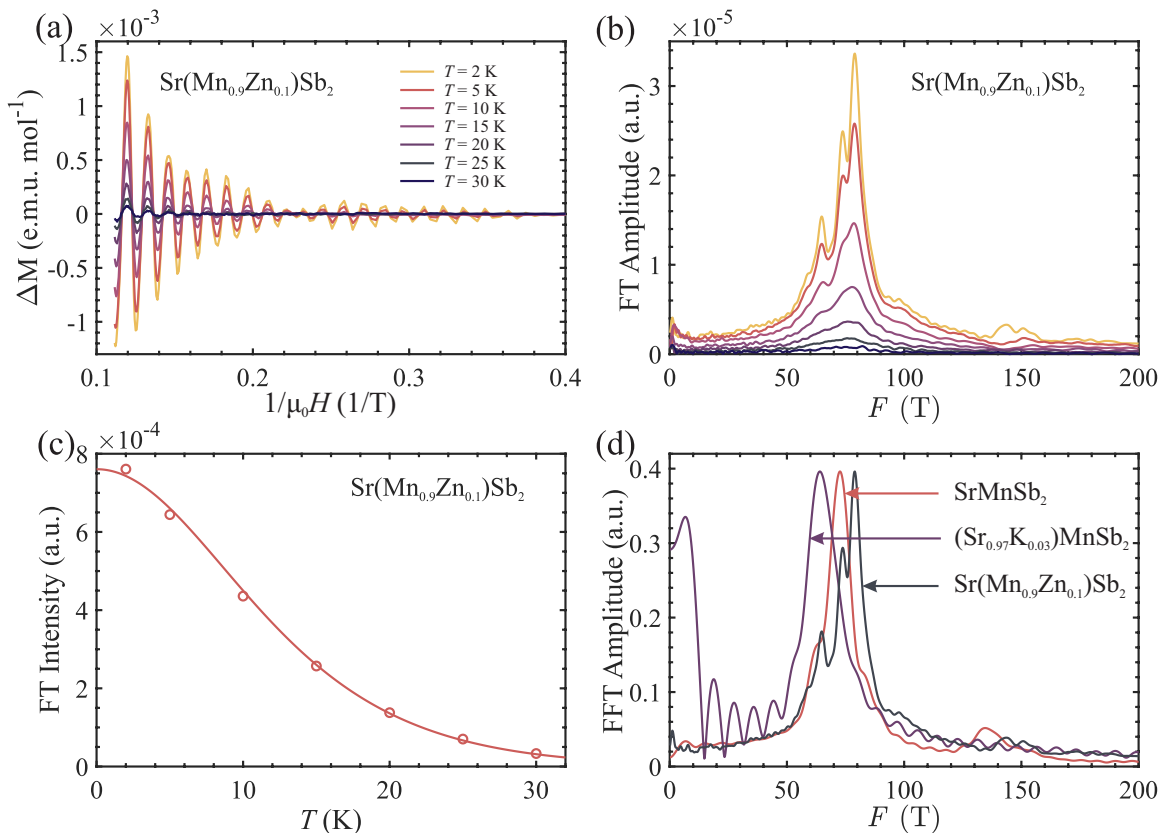


FIG. 3: (a) Corrected magnetization versus the inverse applied magnetic field ($1/H$) perpendicular to MnSb planes, $\Delta M(1/H)$, of $\text{Sr}(\text{Mn}_{0.9}\text{Zn}_{0.1})\text{Sb}_2$ at various temperatures, as indicated, showing dHvA oscillations (data were corrected for an FM contribution as discussed in Refs. [10, 11]). (b) Numerical FT spectra obtained from the $\Delta M(1/H)$ data shown in (a). (c) Temperature dependence of the integrated intensity (from 40 to 120 T) of the FT spectra shown in (b). (d) Comparison of FT spectra at $T = 2$ K of the parent compound SrMnSb_2 , and the doped compounds $\text{Sr}(\text{Mn}_{0.9}\text{Zn}_{0.1})\text{Sb}_2$ and $(\text{Sr}_{0.97}\text{K}_{0.03})\text{MnSb}_2$ [11].

sistent with the nominal doping.

X-ray diffraction (XRD) measurements of the $(h00)$ reflections from the surfaces of the crystals were performed on a Bruker D8 Advanced Powder Diffractometer by using $\text{Cu K}\alpha$ radiation. These measurements indicate that the a -axis (corresponding to the crystallographic direction normal to the layers in the $Pnma$ structure) lies parallel to the surface normal of the plate-like crystals.

We note that there are two inequivalent Sb atoms in the unit cell (labelled as Sb1 and Sb2 in Fig. 1). The Sb1 atoms play a prominent role in the topological character of the system, contributing to the formation of linear Dirac bands near the Fermi level (E_F) at the Y-point [6, 8]. The Sb2 atoms are bonded to the Mn to form corrugated MnSb layers, common to a plethora of layered Mn based pnictides with $\text{Mn}Pn$ ($Pn = \text{P, As, Sb, Bi}$). The Sb2 atoms bridge Mn atoms and provide the in-plane Mn-Mn superexchange paths (similar to As sites in BaMn_2As_2 and in other $\text{Mn}Pn$ systems [12]).

Magnetization measurements were performed by using a Physical Property Measurement System (PPMS, Quantum Design) equipped with a vibrating sample magnetometer (VSM). For the temperature-dependent magne-

tization measurements, the samples were cooled down to the desired temperature with or without an applied magnetic field, termed as FC and ZFC, respectively. The temperature-dependent magnetization data were then collected upon warming at 2 K/min and at a fixed field. The magnetic field H was applied either perpendicular to the MnSb layers (i.e., perpendicular to the plate; H_\perp) or the bc MnSb planes (H_\parallel).

To determine the magnetic structures, single-crystal neutron diffraction experiments were carried out on the triple-axis spectrometer (TRIAx) located at the University of Missouri Research Reactor (MURR). The TRIAx measurements operate at an incident energy of $E_i = 14.7$ meV using a pyrolytic graphite (PG) monochromator system and is equipped with a PG analyzer stage. PG filters were placed before and after the second monochromator to reduce higher order contamination in the incident beam achieving a ratio $I_{\lambda/2} : I_\lambda \approx 10^{-4}$. The beam divergence was defined by collimators of $60' - 60' - 40' - 80'$ between the reactor source to a monochromator, monochromator to sample, sample to analyzer, and analyzer to detector, respectfully. Crystals were anchored to the cold tip of the Advanced Research Systems closed-

TABLE I: Lattice parameters a , b , c , the Néel temperature T_N , and the average ordered magnetic moment $\langle gs \rangle$ of the SrMnSb₂, Sr(Mn_{0.9}Zn_{0.1})Sb₂, Sr(Mn_{0.9}Cu_{0.1})Sb₂ (the latter two are denoted as Zn-doped and Cu-doped, respectively)

	SrMnSb ₂ *	Zn-doped	Cu-doped
a (Å)	23.011(4)	23.144(5)	23.144(5)
b (Å)	4.384(5)	4.374(9)	4.364(9)
c (Å)	4.434(7)	4.423 (9)	4.440(9)
T_N (K)	300	205(5)	210(10)
$\langle gs \rangle$ (μ_B)	3.8(2)	3.9(3)	4.0(3)

* The values are compiled from Refs. [8, 10]

cycle helium refrigerator and cooled to a base temperature of 6.7 K samples oriented in their $(0kl)$ scattering plane.

To better understand and rationalize the experimental results of the SrMnSb₂ based materials at the atomic level, we have performed ab-initio density functional theory calculations based on the structure shown in Fig. 1. To introduce chemical substitutions of the Mn site with either Zn or Cu, we considered supercells with various substitution levels, as discussed below. In our DFT calculations, we have employed the generalized gradient approximation (GGA) for the exchange and correlation functional within the projector augmented wave (PAW) method [13, 14] in conjunction with spin-orbit coupling (SOC), as implemented in the Vienna Ab-initio Simulation Package (VASP). We have used the experimental lattice parameters [15] see Table I for the parent-SrMnSb₂ having space group of $Pnma$ and relaxed the structure for both atomic positions and lattice parameters. The theoretically optimized lattice parameters of parent-SrMnSb₂ are $a = 23.004$, $b = 4.4065$, and $c = 4.4439$ Å. To be as close as possible to the experimental 10% substitution, we consider 12.5% substitution of Cu and Zn, by exchanging one Mn atom in a $2 \times 1 \times 1$ supercell. For the supercell calculations we used the experimental lattice parameters. We also explore the higher 25% substitution by exchanging one of the four equivalent Mn sites in the chemical cell. The convergence criterion for the self-consistent calculations is 10^{-7} eV for the total energy per supercell, and an energy cutoff of 330 eV is used for the electronic wave functions. A Γ -centered grid of $4 \times 12 \times 12$ k-points is used for Brillouin zone sampling in the self-consistent calculations.

III. RESULTS AND DISCUSSION

Figure 2 (a) shows the temperature dependence of the magnetic susceptibilities at an applied field of $H = 1$ T with H perpendicular to the MnSb planes ($\chi_{\perp}(T) \equiv M_{\perp}/H$) for SrMnSb₂, Sr(Mn_{0.9}Cu_{0.1})Sb₂ and Sr(Mn_{0.9}Zn_{0.1})Sb₂. The step-like feature in $\chi_{\perp}(T)$ of the parent compound has been identified as a transition to the AFM structure depicted in Fig. 1 at $T_N = 300 \pm 3$

K, consistent with previous reports [8, 10]. The doped Sr(Mn_{0.9}Cu_{0.1})Sb₂ and Sr(Mn_{0.9}Zn_{0.1})Sb₂ show a weak feature at lower temperatures suggesting substantially lower $T_N = 200 \pm 10$ and 210 ± 12 K, respectively. We note that spin-wave theory and the T-matrix approximation of a spin- $\frac{5}{2}$ quantum Heisenberg antiferromagnet on a 2D square lattice diluted with spinless vacancies predict $T_N(x) \approx (1 - 2.6x)T_N(0) = 220$ K ($x = 0.1$ is the concentration of Cu/Zn) [16, 17]. This is consistent with our observations of a reduced T_N , including the determination from the neutron diffraction results. Furthermore, the DFT, discussed below, show that the Cu or Zn reside on the Mn site and that both are spinless ($S \approx 0$). This demonstrates that the substitution of Cu or Zn is random at the Mn site, i.e. there is no evidence of substitution of other atoms in the unit cell, and also that there is no apparent aggregation of the dopants. It is interesting to note that $\chi_{\parallel}(T)$ (for H in the bc -plane), shown in Fig. 2 (b), is smooth at all temperatures with no obvious anomalies corresponding to T_N such as those observed in $\chi_{\perp}(T)$. This is typical of quasi two-dimensional (2D) AFM systems for which strong 2D correlations develop at a much higher temperature than that of the 3D transition temperature. Indeed, in SrMnSb₂, 2D AFM correlations are observed up to 560K [11].

Magnetization versus applied field data for H_{\perp} ($M_{\perp}(H)$) (Fig. 2 (c)) at $T = 2$ K shows dHvA oscillations for SrMnSb₂ and Sr(Mn_{0.9}Zn_{0.1})Sb₂ compounds but not for Sr(Mn_{0.9}Cu_{0.1})Sb₂. By contrast, magnetization curves versus applied field parallel to the planes $M_{\parallel}(H)$ at $T = 2$ K (Fig. 2 (d)) for the three samples show linear dependence on H as expected from slight moment canting for typical AFM systems with moments that are oriented perpendicular to the applied field. This 2D behavior of the dHvA oscillations, observed only when the applied magnetic field is perpendicular to the Mn-layer, confirms that small Fermi surface pockets themselves are 2D in nature, forming cylinders along the a -axis.

Figure 3 (a) shows the magnetization of Sr(Mn_{0.9}Zn_{0.1})Sb₂ (for H_{\perp}), after removing a ferromagnetic impurity component (as described in more detail in Refs. [10, 11]) versus the inverse of the applied field $\Delta M(1/H)$ at various temperatures. Direct numerical Fourier transforms (FT) of $\Delta M(1/H)$ yield the FT spectra shown in Fig. 3 (b). Figure 3 (c) shows the temperature dependence of the integrated intensity over the main peaks ($H_{FT} \sim 74$ T) in the FT spectra (integrated from 40 to 120 T). The solid line is obtained by fitting the data to the Lifshitz-Kosevich equation to obtain the charge carrier's effective mass (m^*) as given in Ref. [18]

$$P_{FT} = C \frac{KTm^*/H_{av}}{\sinh(KTm^*/H_{av})} \quad (1)$$

where C is a scale factor and $K = 2\pi^2 k_B m_e / (\hbar e) \approx 14.69$ T/K. H_{av} corresponds to the inverse average of the field window over which the Fourier analysis is performed, such that $H_{av} = [(1/H_{start} + 1/H_{end})/2]^{-1} = 7.2$ T with

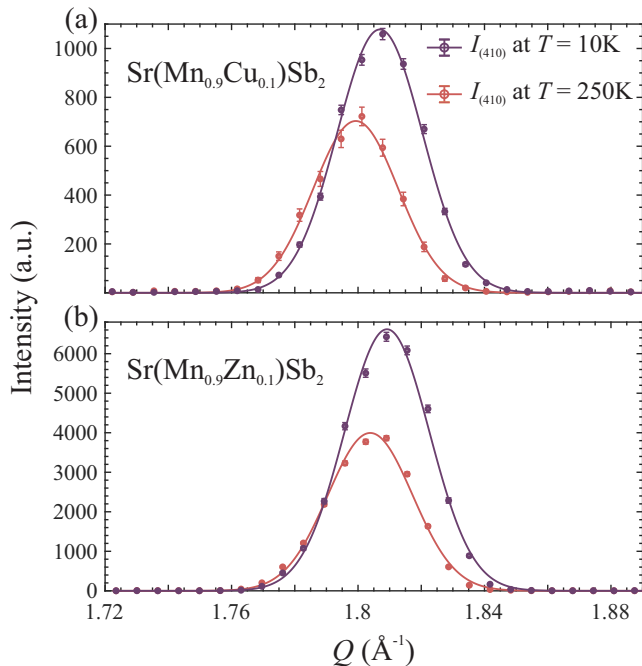


FIG. 4: Longitudinal scan at the (410) peak for (a) $\text{Sr}(\text{Mn}_{0.9}\text{Zn}_{0.1})\text{Sb}_2$ and (b) $\text{Sr}(\text{Mn}_{0.9}\text{Cu}_{0.1})\text{Sb}_2$ at $T = 10$ and 250 K showing temperature-dependent magnetic scattering, consistent with the C-type AFM structure of both systems.

$H_{\text{start}} = 6$ and $H_{\text{end}} = 9$ T. This is the same method used in Ref. [8]. The fit to the data in Fig. 3 (c) yields a very small effective mass of $m^* = 0.03(1)$, which is consistent with the results in Refs. [8, 10], for $(\text{Sr}_{0.97}\text{K}_{0.03})\text{MnSb}_2$.

Figure 3 (d) shows the FT spectra of the dHVA data at $T = 2$ K for the $\text{Sr}(\text{Mn}_{0.9}\text{Zn}_{0.1})\text{Sb}_2$ superimposed with those of SrMnSb_2 , and $(\text{Sr}_{0.97}\text{K}_{0.03})\text{MnSb}_2$ (data adapted from Refs. [10, 11]). We note two observations: first, the FT's center of gravity of $\text{Sr}(\text{Mn}_{0.9}\text{Zn}_{0.1})\text{Sb}_2$ shifts to a higher field compared to that of the parent compound, and second, the FT is more structured and is likely a superposition of a few peaks. The more structured spectra of $\text{Sr}(\text{Mn}_{0.9}\text{Zn}_{0.1})\text{Sb}_2$ suggest a more complicated electronic structure or may result from the inhomogeneity of Zn distribution in MnSb layers.

At base temperature ($T \sim 10$ K), the neutron diffraction data for both the $\text{Sr}(\text{Mn}_{0.9}\text{Zn}_{0.1})\text{Sb}_2$ and $\text{Sr}(\text{Mn}_{0.9}\text{Cu}_{0.1})\text{Sb}_2$ crystals show an intense (010) peak that is not allowed by the chemical symmetry of these crystals, indicating magnetic origin. We also observe significant increase in the intensity of various low index nuclear (210), (410), and (610) Bragg peaks as the temperature is lowered (see Fig. 4). The intensities at (010) and additional intensities on nuclear peaks disappear above the Néel temperature determined from susceptibility measurements, and are consistent with a simple C-type AFM structure similar to that of the parent compound [8, 10]. We note that ($h00$) peaks do not show appreciable temperature dependence, indicating limited or no canting of the moments away from the a -axis (we

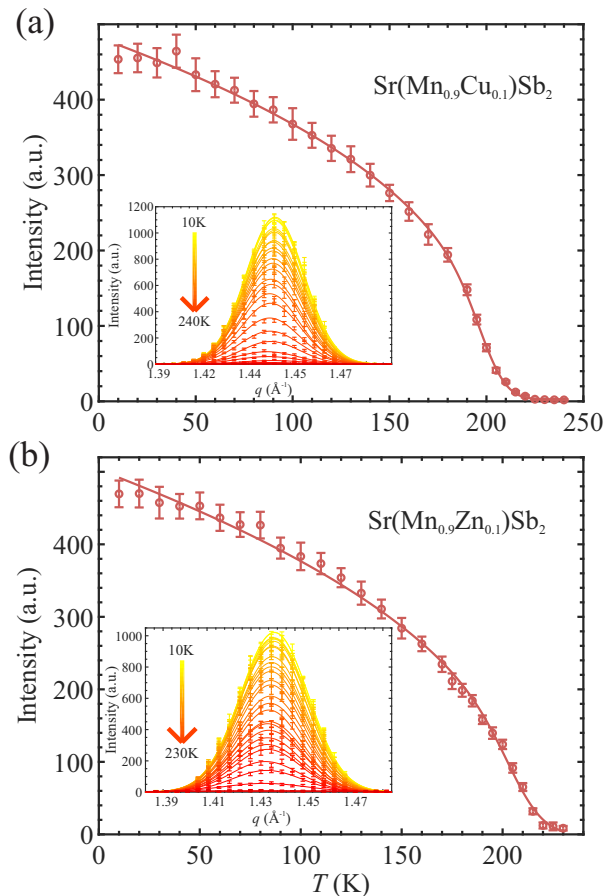


FIG. 5: Integrated intensity versus temperature of the magnetic (010) Bragg peak fitted to a power law $I \propto (1 - T/T_N)^{2\beta}$ (solid line) for (a) $\text{Sr}(\text{Mn}_{0.9}\text{Cu}_{0.1})\text{Sb}_2$ and (b) $\text{Sr}(\text{Mn}_{0.9}\text{Zn}_{0.1})\text{Sb}_2$ with $\beta \approx 0.20$ and 0.22 , and $T_N = 200 \pm 10$ and 210 ± 12 K, respectively. The inset shows the intensity of Bragg reflection (010) as a function of momentum transfer that demonstrates a decreasing trend in intensity as we increase temperature.

estimate an upper limit of a canted moment is less than ~ 0.01 and $0.02 \mu_B$ per Mn site for both the Cu- and Zn-doped systems, respectively). Our detailed analysis of the magnetic peak intensities, assuming the moments are AFM in the plane and all stacked in the same way (C-type AFM), allows us to determine the magnetic moment per Mn site as listed in Table I.

Figure 5 shows the integrated intensities of the (010) magnetic Bragg reflections versus temperature with a fit (solid lines) to a power law $I \propto (1 - T/T_N)^{2\beta}$ and assuming a gaussian distribution of T_N . We assume a distribution of T_N to account for possible inhomogeneities of Zn or Cu in the MnSb planes. The fit to the data shown in Fig. 5 yields with $\beta \approx 0.20$ and 0.22 , and $T_N = 200 \pm 10$ and 210 ± 12 K for the Zn- and Cu-doped crystals, respectively. The insets in Fig. 5 show peak intensity versus longitudinal momentum transfer of the (010) magnetic peak at various temperatures. As described above, the suppression of T_N relative to the parent SrMnSb_2 com-

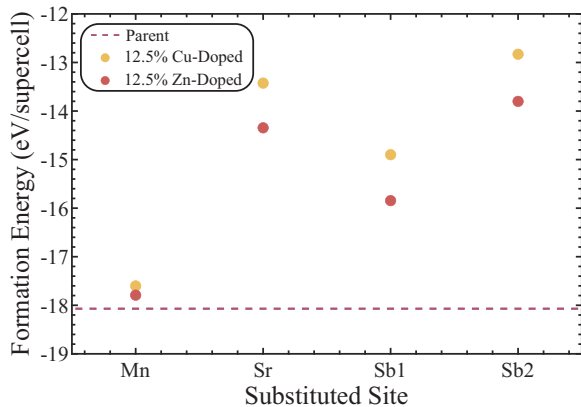


FIG. 6: Formation energy (FE) per supercell (i.e., $2 \times 1 \times 1$) for substitution of various sites (Mn, Sr, Sb1, or Sb2) of the parent SrMnSb₂ with a Cu or Zn atom. The FE of each substitution is compared to that of the parent compound (dashed line), which clearly shows that the Mn site is the most favorable in the formation of the doped system.

found is consistent with site dilution at the level of $\approx 10\%$.

IV. DFT CALCULATIONS

We employ DFT calculations to obtain a better understanding of the evolution of the magnetic properties of Cu and Zn doped SrMnSb₂. First, we perform a detailed study of the parent-SrMnSb₂ to establish the band structure and magnetic structure. Various spin configurations of SrMnSb₂ - such as FM; C-, A-, and G-type AFM - are compared by calculating their ground state energies. C-type AFM configuration is energetically stable, but the energy difference between G-type and C-type AFM is very small ~ 1.29 meV/Mn, consistent with quasi 2D magnetism, as discussed previously [10]. We also compare the ground state energy of the C-type structure with moments aligned either along the *a*, *b*, or *c*-axis. The energy difference between Mn-moment along the *b*- and *c*-axis (within the MnSb-layer) is very small (≈ 0.03 meV/Mn) with an insignificantly lower value for the moment along the *b*-axis. The energy is the lowest for moment orientation perpendicular to the Mn layer (i.e., along the *a*-axis), consistent with the experimentally determined C-type AFM structure (See Table II for more details).

We employ similar calculations to the 12.5% Cu- and Zn-doped systems with $2 \times 1 \times 1$ -supercell, as shown in Fig. 1. As discussed above regarding the reduced T_N , it is justified to assume that Cu and Zn substitute the Mn site only. To confirm that, we conducted formation energy calculations of a supercell with Cu or Zn in the Mn, Sr, Sb1, and Sb2 sites and found that the lowest energy is achieved in the substitutions of the Mn site (see Fig. 6 showing Mn site substitution has the lowest formation energy). The formation energies are calculated

TABLE II: The energy difference between C-Type parent, Cu-, and Zn-doped systems with Mn-moment aligned along the *a*-axis and *b*-axis ($\Delta E_{ab} \equiv E_{b\text{-axis}} - E_{a\text{-axis}}$), and magnetic moment of Mn. Note that for the 25% Cu-doped system, the magnetic moment flops into the Mn-plane.

Systems	ΔE_{ab} (meV/Mn)	Mn-moment (μ_B /Mn)
Parent	0.23	3.75
12.5% Cu-Doped	0.15	3.84
25% Cu-Doped	-0.75	3.73
12.5% Zn-Doped	0.27	3.83
25% Zn-Doped	1.6	3.78

by subtracting total energies of the elements with the appropriate content from the total energy of the doped compound. This further justifies our ensuing detailed calculations by placing the Cu or Zn substitutions only on the Mn site.

We find that the C-type AFM structure is also the most stable configuration in the substituted samples. Based on the observations of the parent compound, we compared the ground state energies of doped systems in the C-type AFM structure with Mn-moment along the *a*- and *b*-axis only. Table II lists the ground-state energy differences for the two spin directions. From the energy differences between Mn-moment aligned along the *a*-axis and *b*-axis (ΔE_{ab}) of all the systems, we find that Mn-moment is aligned along the *a*-axis for 12.5% Zn/Cu-doped systems. Similar considerations for the higher concentration of 25% (chemical unit cell with substitution of one Mn with Cu or Zn) show that the C-type AFM is preserved with Mn-moment along the *a*-axis for the Zn-doped, whereas for the Cu substitution, it is reoriented along the *b*-axis. This is expected as Mn²⁺, with an effective total orbital moment $L \approx 0$, exhibits relatively weak single-ion anisotropy, and thus is susceptible to spin-flop either by external magnetic field or by local atomic environment.

The calculated average Mn-moment in the parent, 12.5% Cu-doped, and 12.5% Zn-doped systems is 3.75, 3.84, and 3.83 μ_B per Mn atom, respectively, agreeing with the presented experimental values (see Table I). Our calculations also determine that the average magnetic moments on the Cu and Zn sites are both negligible with 0.02 μ_B per Cu and 0.01 μ_B per Zn. These results imply that effectively Cu⁺ substitutes the Mn²⁺ site, and Zn⁰ or Zn²⁺ substitutes the Mn²⁺ site.

Figure 7 shows the density of states (DOS) of the parent and 12.5% Zn/Cu doped systems. The Fermi level of the parent compound resides in a narrow minimum of the DOS consistent with the semi-metallic (or narrow semi-conducting) character of SrMnSb₂. Upon Cu/Zn substitution, the Fermi level shifts into the valence band (VB). The Cu-doped system has a slightly higher DOS at the Fermi level compared to the Zn-doped system.

Atom projected DOS (Fig. 7 (b-d)) of each system is

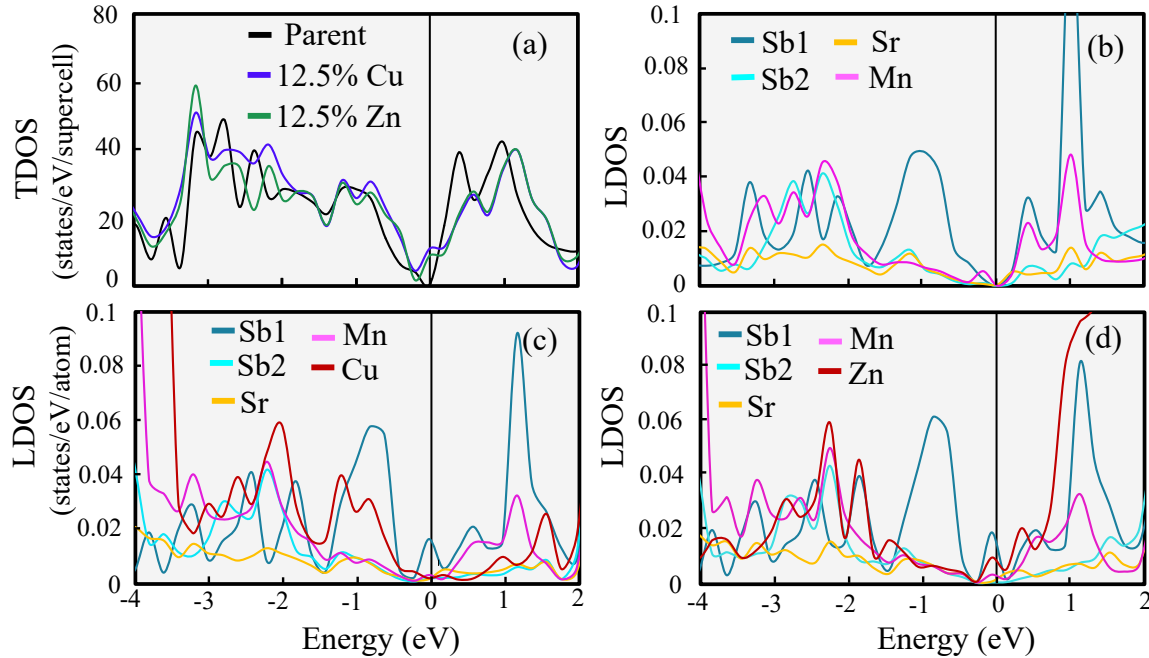


FIG. 7: (a) A superposition of the total density of states (DOS) of SrMnSb_2 and 12.5% Cu/Zn-doped systems showing the parent’s semi-metallic character and the shift of the Fermi level ($E_F = 0$) by electron doping into the valence band, rendering the Cu/Zn doped systems metallic. (b) Atom specific partial DOS contributions to the total DOS for the parent compound. Partial DOS curves with trends as a function of energy imply hybridization (for instance, Sb2-Mn) that have been implicated in invoking the in-plane Mn-Mn superexchange via p -states of Sb2 and d -states in Mn. Note the substantial contribution of Sb1 to DOS near the Fermi level in the conduction and valence bands. Energy bands associated with Sb1 have been implicated as the ones rendering the system “topological.” (c) Same as (b) for the $2 \times 1 \times 1$ supercell with substitution of one Mn with Cu atom (12.5% sample) showing the strong partial contribution to DOS by Cu and Sb1 at and near the Fermi level. (d) Same as (c) for the Zn-doped sample with a strong contribution to the DOS from Sb1 and Mn.

also compared to ascertain the major contribution of each element at and near E_F . It is evident that for SrMnSb_2 , Sb1 p -states are the main contributor to the DOS near the conduction and valence bands. Figure 7 (b) shows hybridization of Sb1 p -states with Mn d -states above the Fermi level (~ 0 to 1 eV range), whereas Mn hybridizes strongly with Sb2 below the Fermi level (~ -2 to -4 eV range). It is interesting to note some hybridization of Cu and Sb1 states in this energy range, which is absent in the Zn doped system. This indicates different effects of Cu- and Zn- impurities on the electronic structure pointing out the possibility that a Cu site introduces a larger cross-section than Zn site for scattering free carriers in the Sb1 layer. Such scattering may affect the lifetime of a free carrier (i.e., shorten the mean free path), which is detrimental to the dHvA effect, and can rationalize the absence of the dHvA effect for Cu doped compounds.

Figure 8 shows the band structures of the parent, Cu-doped, and Zn-doped systems at concentration 12.5% (replacing one Mn with Cu/Zn in $2 \times 1 \times 1$ -supercell), and at 25% (replacing one Mn with Cu/Zn in the chemical unit cell). Figures 8 (a) and (b) show band structure calculations of the SrMnSb_2 using the chemical unit cell and $2 \times 1 \times 1$ -supercell, respectively to ensure invariance of

results to the choice of cell size. All features in the band structure of $2 \times 1 \times 1$ -supercell (Fig. 8 (b)), including the high symmetry points, are the same as those calculated for the chemical unit cell bands (Fig. 8 (a)), and agrees well with previous reports [9, 19]. In the band structure of SrMnSb_2 (Fig. 8 (a-b)), the Fermi level touches the VB at the G-point, and the CB at the M-point. There is a Dirac cone near the Y-point, albeit with a band-gap of ~ 0.19 eV due to spin-orbit coupling, and a 0.31 eV gap at the Y-point (for more detailed band structure around the Y-point, see Fig. 9 (a)). The calculation here suggests that the Fermi surfaces of SrMnSb_2 are hole-like (or have hole-pockets) at the G-point and electron like (or electron pockets) at the Y- and M-points [20]. However, recent Hall coefficient measurement, ARPES, and quantum oscillations of SrMnSb_2 are consistent with a lower Fermi level and a hole-like pocket at the Y-point [9, 10].

Figures 8 (c) and (d) show the band structures of the 12.5% of Cu/Zn substituted in a $2 \times 1 \times 1$ -supercell, showing that Cu and Zn substitutions change the features at the high symmetry points differently. The doped systems are metallic-like in nature, as also demonstrated above from the DOS. Cu substitution mostly affects the bands

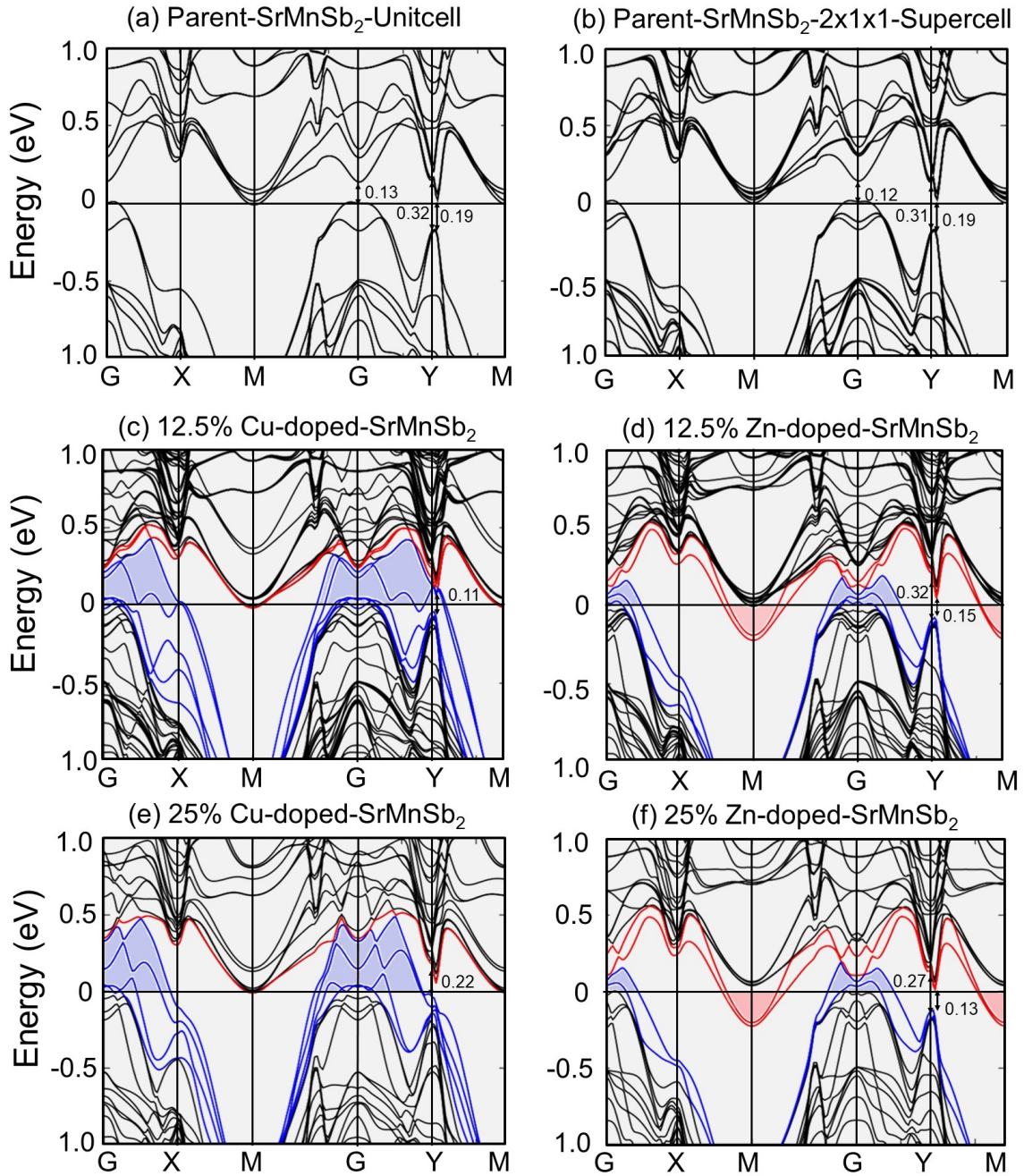


FIG. 8: Band structures of (a) a chemical unit cell and (b) a $2 \times 1 \times 1$ -supercell of parent SrMnSb_2 , and (c, e) doped systems with 12.5%, 25% Cu, and (d, f) 12.5%, 25% Zn. The shaded light blue and light red colors represent the regions that are shifted upon doping from the VB to CB (hole-pockets) and from CB to VB (electron pockets), respectively. The Fermi level is at $E = 0$ eV. The gap of the Dirac cone and the gap at the Y-point is shown using an arrow. Red and blue bands around the Fermi level are the crossed bands from CB to VB and vice-versa, respectively, due to the doping effect.

at G, Y, and X-points, whereas Zn affects only the M and G-points. Most interesting is the fact that the Dirac cone near the Y-point is practically not affected by Zn-doping, whereas it is significantly changed with Cu-doping, as can be clearly seen in Fig. 9. Figure 8 (d) shows that the 25% Cu/Zn-doping has almost the same effects on the

energy bands as the 12.5% doping. Cu substitution affects the Y-point significantly enough to distort the Dirac cone and diminish the dHvA oscillations, as observed experimentally.

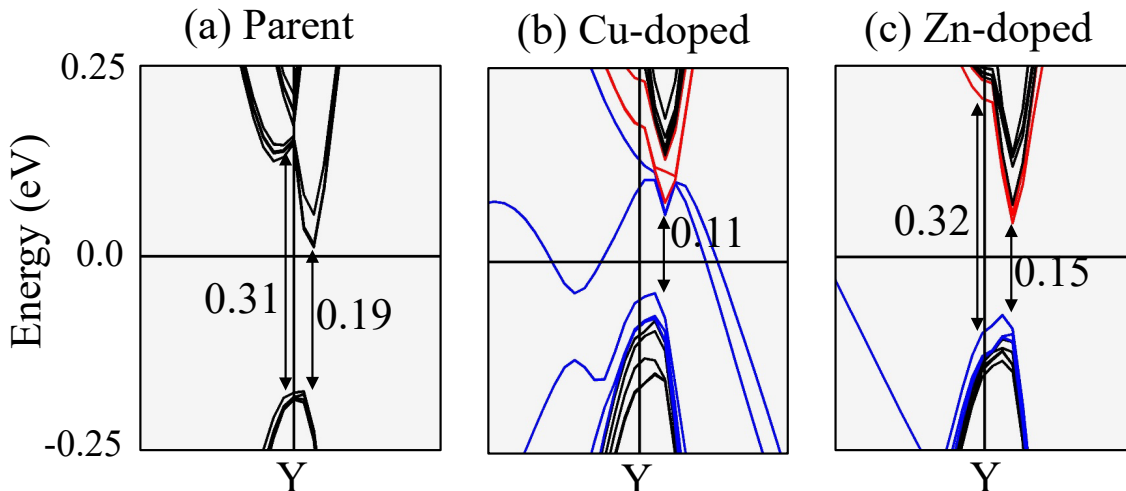


FIG. 9: Band structures calculations focused on the Y-point near the Fermi level for (a) parent, (b) 12.5% Cu-doped, and (c) 12.5% Zn-doped systems. The gaps at the Dirac cone and the Y-point are indicated by arrows, and the values are in eV. The Dirac feature near Y-point and the corresponding gap in the Zn-doped system, shown in (c), are almost as those of SrMnSb₂, as shown in (a). The Cu-doped system, shown in (b), has significantly distorted bands at the Y-point, making the system less Dirac-like, and likely inhibiting the dHvA effect. Blue solid lines in (b) and (c) show band-crossing at the Fermi level from VB to CB.

V. CONCLUSIONS

We have grown single crystals of Sr(Mn_{0.9}Cu_{0.1})Sb₂ and Sr(Mn_{0.9}Zn_{0.1})Sb₂, and determined their properties using magnetic susceptibility, magnetization versus the applied magnetic field, and neutron diffraction measurements. We find that the Mn²⁺ moments in both systems undergo C-type antiferromagnetic ordering at $T_N = 200 \pm 10$ and 210 ± 12 K, respectively - which is significantly reduced compared to their parent SrMnSb₂ with $T_N = 297 \pm 3$ K. The reduction of T_N with respect to the parent compound is likely caused by dilution effects. Analyzing the neutron diffraction patterns, we find that the magnetic moment per Mn²⁺ is 3.9(3) and 4.0(3) μ_B for the Cu- and Zn-doped systems and slightly larger than that of the parent SrMnSb₂. Magnetization versus applied magnetic field (perpendicular to the MnSb planes) measurements at low temperatures (below ~ 30 K) show oscillations due to the dHvA effect for the Zn-doped system, with features that are slightly modified compared to those of the parent compound. In contrast, the Cu-doped system does not show the dHvA effect.

We also provide DFT calculations including spin-orbit coupling which confirm that Zn and Cu substitute for Mn. DFT predicts C-type AFM order with a magnetic moment that agrees with experiments in the parent, and doped Cu and Zn systems. The calculations also identify the easy a -axis of the magnetic moment in the parent and 12.5% of Cu or Zn compositions. Interestingly, for the 25% Cu content, the calculations predict an easy b -axis C-type antiferromagnet, which has not yet been observed experimentally. Considering that the single-ion

anisotropy is expected to be very weak for an Mn²⁺ (d^5 configuration) with $L \approx 0$, it is likely that the spin direction can be readily flopped by either magnetic field or internal perturbation (i.e., crystal field effects), in this case, apparently exerted by the Cu substitution.

The DFT calculations show that the incorporation of Cu and Zn in SrMnSb₂ causes distortions of the electronic bands at the Fermi level. The calculations yield two distinct behaviors of the Cu and the Zn doped systems that qualitatively rationalize the absence and observation of the dHvA effect, respectively. First, the calculated DOS show that the Cu states are more hybridized with Sb1's p -states and are more abundant near the Fermi level, possibly increasing the carrier scattering, which results in a decrease in the mean free path of the carriers that will suppress the dHvA oscillations. Second, the band structure calculations for the Zn-doped system show that the Y-point, hosting a gapped Dirac cone and being responsible for the dHvA oscillations, is only slightly modified compared to the parent SrMnSb₂. By contrast, the calculations for the Cu-doped system show severe disruption near the Y-point, which may inhibit the occurrence of the dHvA effect.

Acknowledgments

This research was supported by the U.S. Department of Energy, Office of Basic Energy Sciences, Division of Materials Sciences and Engineering. Ames Laboratory is operated for the U.S. Department of Energy by Iowa State University under Contract No. DE-AC02-07CH11358. A

portion of this research used resources at the High Flux Isotope Reactor, a DOE Office of Science User Facility operated by the Oak Ridge National Laboratory.

The theoretical capabilities, specific to electronic (band) structure, magnetic order, and magnetic anisotropy predictions, employed in this work have been developed in Critical Materials Institute, an Energy In-

novation Hub led by Ames Laboratory and funded by the U. S. Department of Energy, Office of Energy Efficiency and Renewable Energy, Advanced Manufacturing Office. R. C. and D. P. would like to acknowledge Ed Moxley for maintaining computational facilities, including the RAMAN cluster and computational software.

-
- [1] J. Park, G. Lee, F. Wolff-Fabris, Y. Y. Koh, M. J. Eom, Y. K. Kim, M. A. Farhan, Y. J. Jo, C. Kim, J. H. Shim, and J. S. Kim, *Phys. Rev. Lett.* **107**, 10.1103/PhysRevLett.107.126402 (2011).
- [2] K. Wang, D. Graf, H. Lei, S. W. Tozer, and C. Petrovic, *Phys. Rev. B* **84**, 220401 (2011).
- [3] K. Wang, D. Graf, L. Wang, H. Lei, S. W. Tozer, and C. Petrovic, *Phys. Rev. B* **85**, 041101 (2012).
- [4] K. Wang, L. Wang, and C. Petrovic, *Appl. Phys. Lett.* **100**, 112111 (2012), arXiv:1204.2256 .
- [5] G. Lee, M. A. Farhan, J. S. Kim, and J. H. Shim, *Phys. Rev. B* **87**, 245104 (2013).
- [6] M. A. Farhan, G. Lee, and J. H. Shim, *J. Phys. Condens. Matter* **26**, 042201 (2014).
- [7] J. Liu, J. Hu, H. Cao, Y. Zhu, A. Chuang, D. Graf, D. J. Adams, S. M. A. Radmanesh, L. Spinu, I. Chiorescu, and Z. Mao, *Sci Rep* **6**, 30525 (2016).
- [8] J. Y. Liu, J. Hu, Q. Zhang, D. Graf, H. B. Cao, S. M. A. Radmanesh, D. J. Adams, Y. L. Zhu, G. F. Cheng, X. Liu, W. A. Phelan, J. Wei, M. Jaime, F. Balakirev, D. A. Tennant, J. F. DiTusa, I. Chiorescu, L. Spinu, and Z. Q. Mao, *Nat. Mater.* **16**, 905 (2017).
- [9] S. V. Ramankutty, J. Henke, A. Schiphorst, R. Nutakki, S. Bron, G. Araizi-Kanoutas, S. Mishra, L. Li, Y. Huang, T. Kim, M. Hoesch, C. Schlueter, T.-L. Lee, A. de Visser, Z. Zhong, J. van Wezel, E. van Heumen, and M. Golden, *SciPost Phys.* **4**, 010 (2018).
- [10] Y. Liu, T. Ma, L. Zhou, W. E. Straszheim, F. Islam, B. A. Jensen, W. Tian, T. Heitmann, R. A. Rosenberg, J. M. Wilde, B. Li, A. Kreyssig, A. I. Goldman, B. G. Ueland, R. J. McQueeney, and D. Vaknin, *Phys. Rev. B* **99**, 054435 (2019).
- [11] Y. Liu, F. Islam, K. W. Dennis, W. Tian, B. G. Ueland, R. J. McQueeney, and D. Vaknin, *Phys. Rev. B* **100**, 014437 (2019).
- [12] F. Islam, E. Gordon, P. Das, Y. Liu, L. Ke, D. L. Abernathy, R. J. McQueeney, and D. Vaknin, *Phys. Rev. B* **101**, 155119 (2020).
- [13] G. Kresse and D. Joubert, *Phys. Rev. B* **59**, 1758 (1999).
- [14] G. Kresse and J. Furthmüller, *Phys. Rev. B* **54**, 11169 (1996).
- [15] E. Blokhin and Villars, Pierre, *The PAULING FILE Project and Materials Platform for Data Science: From Big Data Toward Materials Genome*. (Springer, Cham, 2018).
- [16] A. L. Chernyshev, Y. C. Chen, and A. H. Castro Neto, *Phys. Rev. B* **65**, 104407 (2002).
- [17] R. A. Cowley, *Philosophical Transactions of the Royal Society of London. Series B, Biological Sciences* **290**, 583 (1980).
- [18] M. V. Kartsovnik, *Chem. Rev.* **104**, 5737 (2004).
- [19] C. P. Weber, M. G. Masten, T. C. Ogloza, B. S. Berggren, M. K. L. Man, K. M. Dani, J. Liu, Z. Mao, D. D. Klug, A. A. Adeleke, and Y. Yao, *Phys. Rev. B* **98**, 155115 (2018).
- [20] J. Singleton, *Band Theory and Electronic Properties of Solids* (Oxford University Press, 2001).